Size effect on the oxidation of aluminum nanoparticle: Multimillion-atom reactive molecular dynamics simulations

Ying Li, Rajiv K. Kalia, Aiichiro Nakano, and Priya Vashishta
Collaboratory for Advanced Computing and Simulations, Department of Chemical Engineering and Materials Science, Department of Physics and Astronomy, and Department of Computer Science, University of Southern California, Los Angeles, California 90089-0242, USA

(Received 21 July 2013; accepted 16 September 2013; published online 4 October 2013)

The size effect in the oxidation of aluminum nanoparticles (Al-NPs) has been observed experimentally; however, the mechano-chemistry and the atomistic mechanism of the oxidation dynamics remain elusive. We have performed multimillion atom reactive molecular dynamics simulations to investigate the oxidation dynamics of Al-NPs (diameters, $D = 26$, 36, and 46 nm) with the same shell thickness (3 nm). Analysis of alumina shell structure reveals that the shell of Al-NPs does not break or shatter, but only deforms during the oxidation process. The deformation depends slightly on the size of Al-NP. This reaction from the oxidation heats the Al-NP to a temperature of $T > 5000$ K. Ejection of Al atoms from shell starts earlier in small Al-NPs—at $t_0 = 0.18$, 0.28 and 0.42 ns for $D = 26$, 36 and 46 nm, when they all have the same shell temperature of 2900 K. As the oxidation dynamics proceeds, the total system temperature (including the environmental oxygen) increases monotonically; however, the time derivative of the total temperature, (dT_{system}/dt), reaches a maximum at $t_1 = 0.20$, 0.32 and 0.51 ns for $D = 26$, 36 and 46 nm. At this peak value of (dT_{system}/dt), the shell temperature for the three Al-NPs are 3100 K, 3300 K, and 3500 K, respectively. The time lag between t_1 and t_0 is 0.02, 0.04 and 0.09 ns for $D = 26$, 36 and 46 nm clearly indicates the size effect. [http://dx.doi.org/10.1063/1.4823984]

I. INTRODUCTION

Combustion of aluminum is a subject of great interest in science, engineering, and technology. It has been studied since the last century due to its wide use in the field of solid propellants and explosives. For instance, combustion of micron size Al particles was studied by Dreizin[1] and Jordan *et al.*[2] using different experimental approaches. The effect of temperature on oxidation[3–7] and the effect of oxide shell on the surface[8–15] have been studied extensively, especially for nanosize Al particles. Many different mechanisms have been proposed to explain the combustion behavior of Al nanoparticles (Al-NPs).[16–19]

By adding Al-NPs into micron size particles, numerous experiments have observed the enhanced oxidation reactivity in terms of burning rate,[20,21] flame speed,[22,23] activation energy,[24] ignition sensitivity,[23,25–27] combustion velocity,[25] and agglomeration.[3] Nanosize Al particles have lower melting temperatures than that of micron size particles, because of large surface-to-volume ratio. The combustion rate of Al nano-composites has been observed to increase significantly over micron size Al composites. Several investigators have specifically investigated the size effect on the combustion of Al-NPs.[28,29] Most of them concluded that the smaller the size of Al-NPs is, the higher the reactivity becomes. However, the effect of particle size on reactivity is still controversial. For example, Gan and Qiao[30] have conducted experiments on fuel droplets with nano (~80 nm) and micron (~5 mm and ~25 mm) size Al particles. They found that the combustion is longer and less complete for large agglomerate of nanosuspensions due to the formation of oxide shell on the Al-NPs surface. In a review article, Yetter *et al.*[31] stated that for smaller Al particles, the energy loss per unit volume due to the presence of the same oxide layer thickness is significantly larger.

Besides the above-mentioned experimental studies, there have been numerical simulations of oxidation dynamics of Al-NPs. Campbell *et al.*[32,33] studied the oxidation of aluminum nanoclusters with a parallel molecular dynamics (MD) approach based on dynamic charge transfer among atoms in both microcanonical and canonical ensembles and for atomic and molecular oxygen environments. Alavi *et al.*[34] have simulated the oxidation of Al-NPs using MD with Streitz-Mintmire electrostatic plus (ES+) potential.[35,36] Puri and Yang[37] performed MD simulation to study the thermo-mechanical behavior of nano-Al particles coated with crystalline and amorphous oxide layers. Perron *et al.*[38] have studied the oxidation of multi-grain nanocrystalline (mean grain size = 5 nm) Al surfaces in the temperature range 300–750 K using variable charge molecular dynamics simulations. Structures of γ- and amorphous Al_2O_3 have been investigated using MD and density function theory (DFT) by Gutierrez *et al.*[39,40] Vashishta *et al.*[41] have developed an interaction potential consisting of two- and three-body terms for alumina to simulate the amorphous and liquid phases. Combining Vashishta's potential[41] and embedded atom method (EAM) potential,[42] Wang *et al.*[43] have studied atomistic mechanisms of oxidation in a laser flash heated core (aluminum)-shell (alumina) nanoparticle. In another paper by Wang *et al.*,[44] they studied effects of the

crystalline and amorphous structures of alumina shells on the dynamics of oxidation of an Al-NP.

Despite the extensive experimental and simulation research efforts mentioned above, several key questions remain unanswered. Most important of them are the collective reaction behaviors among particles; and spatially and temporally resolved oxidation dynamics of individual particles at atomic resolution. It is essential to delineate these issues unambiguously and study each factor independently. Regarding the collective reaction, Shekhar *et al.*[45] have investigated the mechano-chemial reaction in the oxidation of three adjacent Al-NPs by initiating the oxidation in the middle nanoparticle and studying the nature and speed of the oxidation front. However, there is no systematic study on the atomistic mechanisms underlying size-dependent oxidation dynamics of individual Al-NPs. This paper focuses on the size dependence of oxidation dynamics rate and that of reaction temperature, as well as the role of oxide shell in Al-NPs oxidation. Here, we report the results of large-scale, parallel MD simulations of the size effect on single Al-NP of diameters $D = 26$, 36, and 46 nm. The rest of the paper is organized as follows. The interatomic interaction potential and the system setup are described in Secs. II and III, respectively. Simulation results are presented in Sec. IV, and conclusions are in Sec. V.

II. INTERATOMIC INERACTION POTENTIAL

The foundation of MD simulations is interatomic potential. The modeling of Al_2O_3 is based on a many-body potential that incorporates ionic and covalent effect through a combination of two- and three-body terms[41]

$$V = \sum_{i<j}^{N} V_{ij}^{(2)}(r_{ij}) + \sum_{i<j<k}^{N} V_{jik}^{(3)}(\vec{r}_{ij},\vec{r}_{ik}), \tag{1}$$

where N is the number of atoms in system.

The two-body interatomic interactions include effects of steric repulsion, Coulomb interaction, charge-dipole interaction, and Van der Waals interaction, as given below:

$$V_{ij}^{(2)}(r) = \frac{H_{ij}}{r^{\eta_{ij}}} + \frac{Z_i Z_j}{r} e^{-r/r_{1s}} - \frac{D_{ij}}{r^4} e^{-r/r_{4s}} - \frac{w_{ij}}{r^6}. \tag{2}$$

The three-body interatomic interaction reflects the covalent effects through bond-bending and bond-stretching terms

$$V_{jik}^{(3)}(\vec{r}_{ij},\vec{r}_{ik}) = B_{jik}\exp\left(\frac{\xi}{r_{ij}-r_0} + \frac{\xi}{r_{ik}-r_0}\right) \times \frac{(\cos\theta_{jik} - \cos\theta_0)^2}{1 + C_{jik}(\cos\theta_{jik} - \cos\theta_0)^2} \quad (r_{ij}, r_{ik} \le r_0). \tag{3}$$

In Eq. (2), H_{ij} is the steric repulsion strength; Z_i is the effective charge in units of the electronic charge, e; D_{ij} represents the charge-dipole strength; and w_{ij} is the strength of Van der Waals attractions. η_{ij} is the exponent of the steric repulsion, and r_{1s} and r_{4s} are the screening lengths for the Coulomb and charge-dipole interactions, respectively. r_{ij} is the distance between any two atoms in the system. In Eq. (3), the three-body interaction, B_{ijk} is the strength of the three-body interaction, θ_{ijk} is the angle formed by vectors r_{ij} and r_{ik}, and r_0 is the cutoff distance for the three-body interaction.

This potential has been validated by comparing the MD results for structural and mechanical properties of both crystalline and amorphous alumina with the experimental data.[41]

For aluminum in the core of the nanoparticle, we use the EAM form of the potential[42]

$$E = \sum_{i}^{N} E_i, \tag{4}$$

where E_i is the energy of atom i

$$E_i = \frac{1}{2}\sum_{j} \phi(r_{ij}) + F_i(\bar{\rho}_i). \tag{5}$$

The first term in Eq. (5) describes the electrostatic interaction between atom i and its neighboring atoms j. The second term describes the attractive interaction which models placing a positively charged atom in the electron density due to the free valence sea of electrons created by the host system of atoms. The embedding function $F_i(\bar{\rho}_i)$ is a function of superimposed charge densities $\bar{\rho}_i$, due to the charge density distribution of neighboring atoms

$$\bar{\rho}_i = \sum_{j} \rho(r_{ij}), \tag{6}$$

where $\rho(r_{ij})$ is the pair-wise electronic density as a function of the distance r_{ij} between atom i and atom j, but without angular dependency.

In the case of Voter-Chen's EAM expression, the pair-wise electronic interaction is taken to be a Morse potential

$$\phi(r) = D_M\{1 - \exp[\alpha_M(r - R_M)]\}^2 - D_M, \tag{7}$$

where D_M and R_M define the depth and position of the minimum, respectively. α_M is a measure of the curvature at the minimum. The density function is a hydrogenic *4s* orbital with a relative normalization factor added to ensure the monotonicity

$$\rho(r) = r^6(e^{-\beta r} + 2^9 e^{-2\beta r}), \tag{8}$$

where β is an adjustable parameter.

In order to implement the EAM in MD with $O(N)$ scaling, both $\phi(r)$ and $\rho(r)$ are truncated at cutoff r_{cut} using

$$h(r) = h(r) - h(r_{cut}) + \frac{r_{cut}}{m}\left[1 - \left(\frac{r}{r_{cut}}\right)^m\right]\left(\frac{dh}{dr}\right)_{r=r_{cut}}, \tag{9}$$

where $h(r)$ can be $\phi(r)$ or $\rho(r)$, and $m = 20$.

To describe the oxidation of Al, a bond-order based interpolation scheme is proposed to smoothly interpolate the two potentials in order to guarantee the stability of the interface and the energy conservation.[42] Mathematically, the total

potential energy of the system can be written as the sum of the potential energy of all aluminum atoms and that of all oxygen atoms

$$E_{tot} = \sum_i E_i = \sum_{i(Al)} E_i + \sum_{i(O)} E_i. \tag{10}$$

The potential energy of each Al atom i is a weighted average between Vashishta's potential for alumina and the EAM

$$\begin{aligned} E_i &= E_{\text{Vashishta},i} \cdot f + E_{\text{EAM},i} \cdot (1-f) \\ &= \left(\frac{1}{2}\sum_{j\neq i} V_{ij}^{(2)}\right)\cdot f + \left(\frac{1}{2}\sum_{j\neq i}\phi(r_{i,j}) + F\left(\sum_{j\neq i}\rho(r_{i,j})\right)\right)\cdot(1-f), \end{aligned} \tag{11}$$

where f is the weighting factor as a function of the oxidation degree n_i° of atom i

$$f(n_i^\circ) = \begin{cases} 0 & n_i^\circ \leq 0 \\ \frac{1}{2}\left(\sin((n_i^\circ - 0.5)\cdot\pi) + 1\right) & 0 < n_i^\circ < 1 \\ 1 & n_i^\circ \geq 1. \end{cases} \tag{12}$$

The oxidation degree n_i° of atom i is

$$n_i^\circ = \sum_k \Theta(r_{ik}), \tag{13}$$

where $\Theta(r_{ik})$ is a continuous function that counts the degree of oxidation according to the distance of the considered aluminum atom to a neighboring oxygen atom

$$\Theta(r) = \begin{cases} 0 & r \leq R_\alpha - D_\alpha \\ 1 - \dfrac{r - R_\alpha + D_\alpha}{2D_\alpha} + \dfrac{\sin(\pi(r - R_\alpha + D_\alpha)/D_\alpha)}{2\pi} & R_\alpha - D_\alpha < r < R_\alpha + D_\alpha \\ 1 & r \geq R_\alpha + D_\alpha, \end{cases} \tag{14}$$

here we use $R_\alpha = 3.0$ Å and $D_\alpha = 0.5$ Å.

The interpolated potential was validated by comparing the MD results for the structure of several Al_xO_y small clusters with the corresponding quantum mechanical results.[46] We have also checked the structural and dynamical stability of interface between the aluminum core and the alumina shell once they are put together in the initial configuration of the aluminum nano-particles.

III. SYSTEM SETUP FOR REACTIVE MOLECULAR DYNAMICS SIMULATIONS

The initial setup for the oxidation simulation is as follows (see Table I). The Al-NP diameters are chosen to be $D = 26$, 36 and 46 nm, with 3 nm thick amorphous alumina shell. The metallic Al core is cut from crystalline Al at 300 K. The amorphous shell is prepared by first heating the crystalline alumina, and then slowly quenching the molten alumina into amorphous alumina at 300 K, and then, from the amorphous alumina, removing the outer and inner concentric parts accordingly to retain an oxide layer of 3 nm thick. After combining the crystalline aluminum core and amorphous alumina shell structure together, the single Al-NP is relaxed and thermalized before it is put into an oxygen environment.

The following relaxation procedure is performed for the Al-NP assembled after putting the core (aluminum) and shell (amorphous alumina) together. The reactive MD was run on the Al-NP for 30 ps, in microcanonical ensemble, to form and stabilize the aluminum/alumina interface. Figure 1(a) displays the radial temperature distribution during preparation of 26 nm Al-NP system. We plot temperature within a 10 Å thick spherical shell as a function of radial distance R. The red curve in Fig. 1(a) shows the temperature profile at 30 ps, which is the end of interface-formation process. The shell temperature is higher than core and the environmental oxygen because of the shell reconstruction. The Al-NP is then quenched to 5 K (blue curve in Fig. 1(a)) and the whole system is gradually heated to 300 K (as shown in time sequence of temperature profiles from cyan to green to orange in Fig. 1(a)).

In order to start the oxidation dynamics in the Al-NP, velocity scaling is performed to preheat nanoparticle from 300 K to 1100 K in steps of 100 K (see Fig. 1(b)). In each step, the Al-NP is heated at a constant heating rate, followed by thermalization for 0.1 ns during each interval. During the Al-NP heating, the oxygen environment is kept at 300 K as shown in Fig. 1(b). After the preheating, systems undergo oxidation for 1 ns in microcanonical ensemble. Exactly the same procedure is applied to $D = 36$ and 46 nm Al-NPs.

TABLE I. Reactive molecular dynamics simulation setup for aluminum (core) and amorphous alumina (shell) nanoparticles in oxygen environment.

Particle diameter (nm)	Shell thickness (nm)	No. of core Al atoms	No. of shell Al_2O_3 atoms	No. of environmental oxygen atoms	Total no. of atoms in system	Simulation box size (nm)
26	3	252 288	440 106	237 264	929 658	52
36	3	851 423	897 290	802 498	2 551 211	72
46	3	1 979 315	1 529 708	1 889 162	5 398 185	92

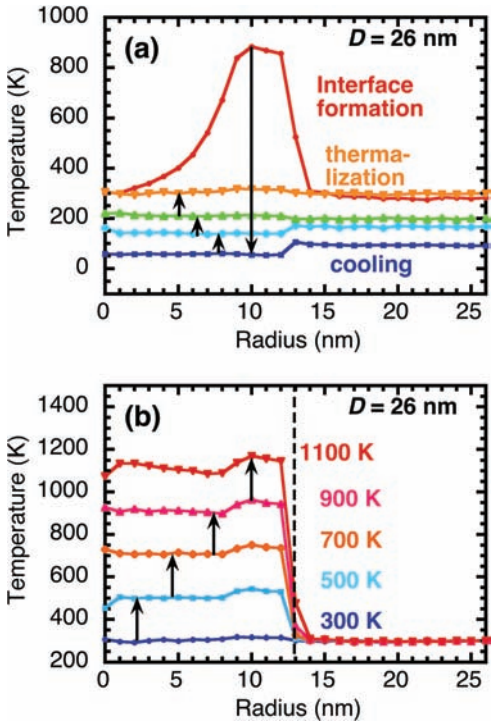

FIG. 1. Radial temperature profile of $D = 26$ nm Al-NP during (a) preparation of aluminum core and alumina shell system, and (b) preheating of the system to 1100 K. The dashed line indicates the interface between the Al-NP and environmental oxygen. The arrows indicate the time sequence of the preparation and preheating.

IV. RESULTS FROM THE ANALYSIS REACTIVE MOLECULAR DYNAMICS SIMULATIONS

A. Oxidation dynamics of three Al-NPs

To visualize the reaction process of the three Al-NPs, Figs. 2–4 show snapshots of the central slice for $D = 26$, 36 and 46 nm Al-NPs at 0.0, 0.2, 0.4, 0.6, 0.8 and 1.0 ns, respectively. Blue color represents environmental oxygen. Green and black colors indicate the oxygen and aluminum atoms, respectively. In the alumina shell, the red color represents the core aluminum in the initial configuration. The oxidation process starts after the initial conditions are set up (core and shell preheated to 1100 K). As the oxidation begins, due to

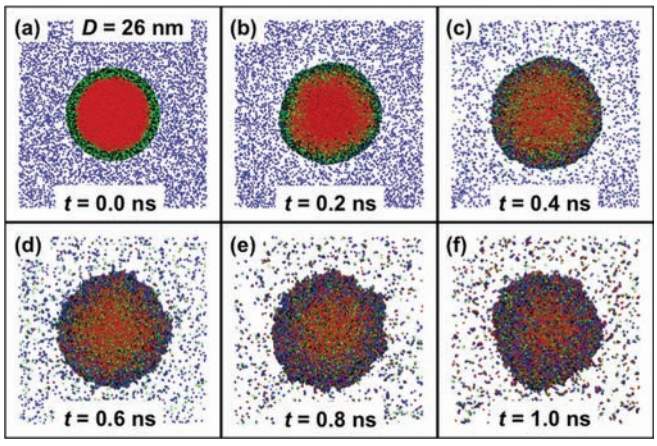

FIG. 2. Snapshots of the central slice for $D = 26$ nm Al-NP at time = 0.0, 0.2, 0.4, 0.6, 0.8, and 1 ns.

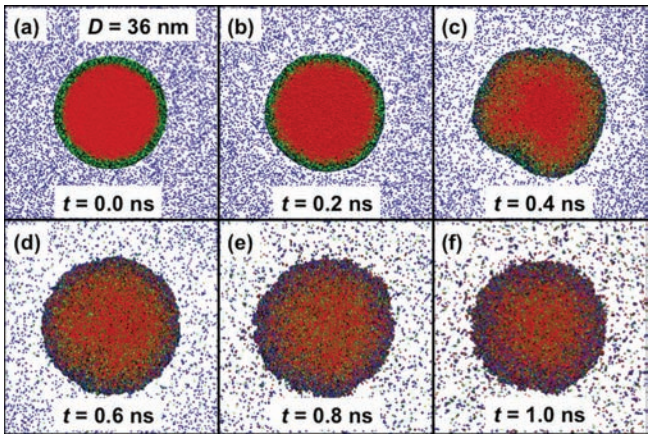

FIG. 3. Snapshots of the central slice for $D = 36$ nm Al-NP at time = 0.0, 0.2, 0.4, 0.6, 0.8, and 1 ns.

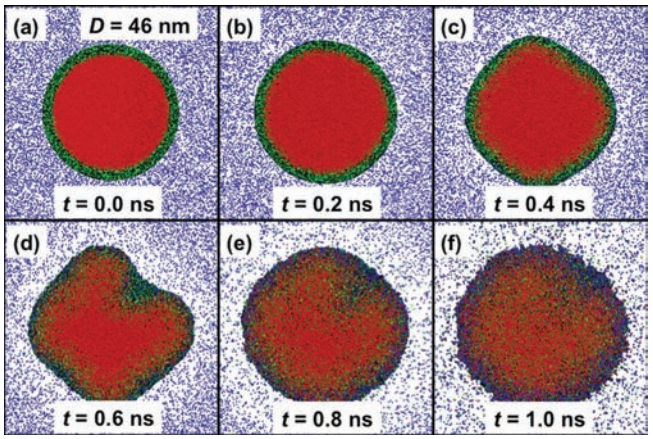

FIG. 4. Snapshots of the central slice for $D = 46$ nm Al-NP at time = 0.0, 0.2, 0.4, 0.6, 0.8, and 1 ns.

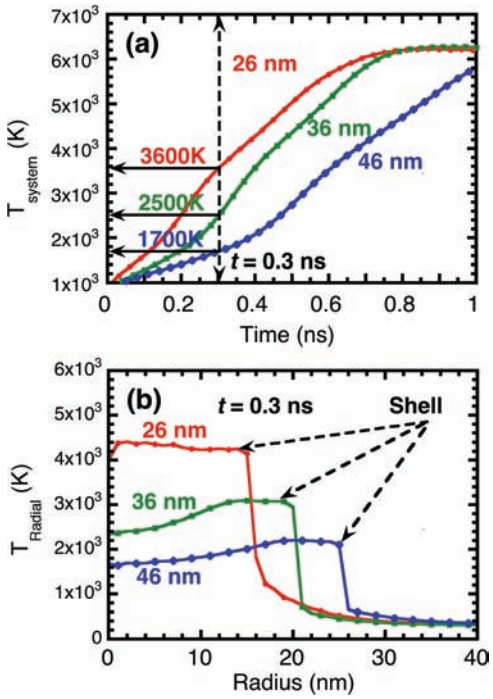

FIG. 5. (a) Temperature of the system (i.e., Al-NP and the environmental oxygen) during the oxidation as a function of time for $D = 26$, 36, and 46 nm. (b) Radial temperature of the three Al-NPs at time 0.3 ns. Position of the alumina shell is indicated by arrows.

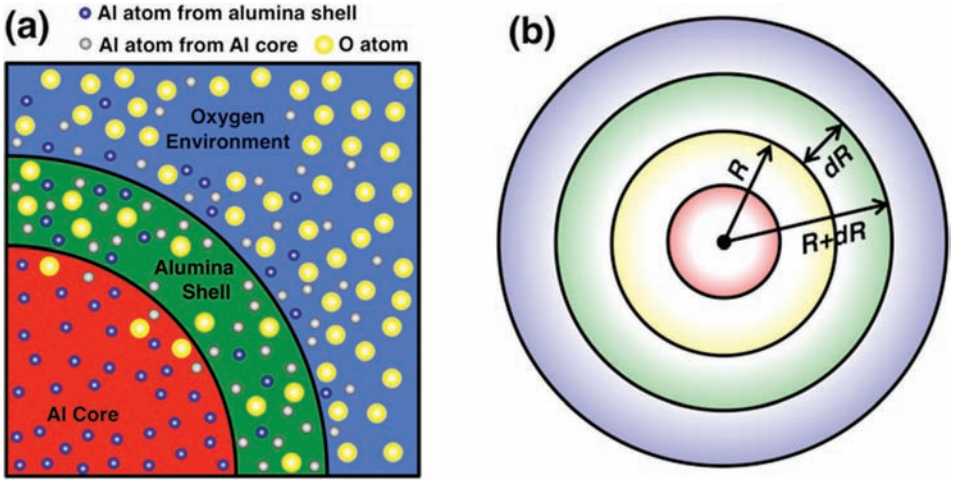

FIG. 6. (a) Schematic of a quarter slice of the whole system. Dark blue, grey, and yellow circles are aluminum atoms from alumina shell, aluminum atoms from aluminum core, and oxygen atoms, respectively. (b) Local concentration is calculated at a distance R by averaging the concentration within a spherical shell of thickness $dR = 10$ Å at radius R from the center of the nanoparticle.

the molten core expansion at 1100 K, the size of the Al-NP grows larger than its initial size.

No shell breaking or shattering of the shell is observed in the oxidation process; only the deformation of Al-NP is observed. From the extent of the core and shell deformation, reaction is apparently more intense for $D = 26$ nm Al-NP than $D = 36$ and 46 nm Al-NPs.

B. Temperature profile of three Al-NP systems

To determine the size dependence on oxidation reactivity of Al-NPs, we study the heat release for all three systems by plotting temperature of whole systems as functions of time showing in Fig. 5(a). Significant amount of heat is produced as a result of oxidation within the nanoparticles in all three systems. The radial temperature distribution of the three systems at 0.3 ns is shown in Fig. 5(b). Temperature at the center of the core is higher than the shell temperature for the smallest system ($D = 26$ nm) as shown in Fig. 5(b). However, the temperature at the center of the core is lower than the shell temperature at 0.3 ns for larger systems ($D = 36$ and 46 nm). Comparison between radial temperature distribution and global temperature of all systems (at time less than 0.3 ns) shows that the shell temperature is higher than the average temperature of the system, which indicates that oxidation at core-shell interface dominates the heat release of the whole system at early stage.

C. Local aluminum atoms concentration

In order to study the distribution of aluminum atoms inside Al-NPs, we calculate local concentration of aluminum atoms from their two different origins, i.e., those from the alumina shell and from the aluminum core (see Fig. 6(a)). Local concentration at distance R from the center of Al-NP is calculated by averaging the concentration within a spherical shell of thickness $dR = 10$ Å. We compute three concentrations as follows:

$$C_{\mathrm{Al}} = \frac{n_{\mathrm{Al}}}{n_{\mathrm{total}}}, \tag{15}$$

$$C_{\mathrm{Al}}^{\mathrm{shell}} = \frac{n_{\mathrm{Al}}^{\mathrm{shell}}}{n_{\mathrm{total}}}, \tag{16}$$

$$C_{\mathrm{Al}}^{\mathrm{core}} = \frac{n_{\mathrm{Al}}^{\mathrm{core}}}{n_{\mathrm{total}}}. \tag{17}$$

C_{Al} is the local concentration of Al, $C_{\mathrm{Al}}^{\mathrm{shell}}$ is the local concentration of Al from alumina shell, and $C_{\mathrm{Al}}^{\mathrm{core}}$ is the local concentration of Al from aluminum core. Here n_{total} is the total

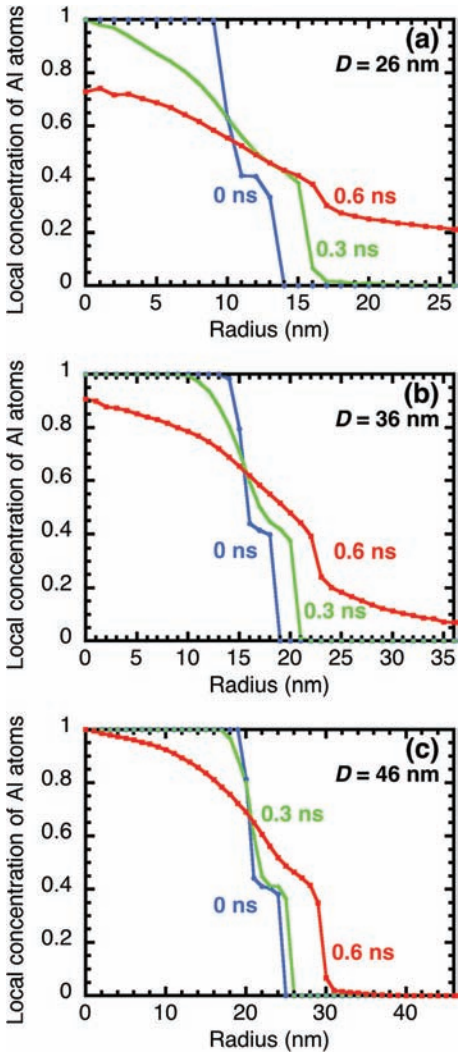

FIG. 7. Local concentration of Al atoms, C_{Al} Eq. (15), at 0 ns, 0.3 ns and 0.6 ns for (a) $D = 26$ nm, (b) $D = 36$ nm and (c) $D = 46$ nm.

number of atoms, n_{Al} is the total number of Al atoms, n_{Al}^{shell} is the number of Al atoms from alumina shell, n_{Al}^{core} is the number of Al atoms from aluminum core at distance R from the center of Al-NP within a spherical shell of thickness $dR = 10$ Å.

Figure 7 shows C_{Al}as function of radius R for time $t = 0$, 0.3 and 0.6 ns for $D = 26$, 36 and 46 nm. In Figs. 7(a)–7(c), at 0 ns, shown in blue lines, there are shoulders around $R = 10$–13, 15–18, and 20–23 nm, respectively. These shoulders reflect the core-shell structure of Al-NPs. Namely, the center part, up to $R = 10$, 15 and 20 nm, respectively, for the three systems, is pure Al. The shell part is Al_2O_3 extends for 3 nm beyond the core. There are no Al atoms beyond the shell radius of the three systems. As time progresses, these shoulders become less pronounced indicating the intermixing of atoms between shell and core.

To distinguish origin of Al atoms, Figs. 8 and 9 show C_{Al}^{shell} and C_{Al}^{core}, respectively. In Fig. 8, the movement of shell Al atoms is observed from the radial distribution at different times. At 0 ns, blue lines, the local concentration is 0.4, reflecting the composition of Al_2O_3. At 0.3 ns, green lines, the alumina shells have moved outwards and become wider due to the expansion of the molten core. For $D = 26$ nm, more Al atoms spread inwards, which is not observed in $D = 46$ nm until 0.6 ns. At 0.6 ns, red lines, more shell Al atoms spread outwards than inwards for $D = 26$ and 36 nm. At times beyond 0.6 ns, the same behavior is seen in $D = 46$ nm.

In Fig. 9, at 0 ps, blue lines, the center part is pure (metallic) Al, while there is no core aluminum in alumina shell or oxygen environment. At 0.6 ns, red lines, the core Al spreads outward. The core Al atoms in $D = 26$ nm moves outwards earlier in time than other systems at the same instant.

D. Formation of Al_xO_y clusters

To understand the oxidation in the core-shell region for three different sizes of Al-NPs, we next investigate the chemical composition of oxide clusters using fragment analysis. As the oxidation starts, the aluminum oxide clusters with a variety of aluminum-oxygen ratios have been found both in simulations[33,47] and experiments.[48–50] Here, we take the fragment as the atoms that are covalently bonded. Except the large fragments (those having over a thousand atoms,

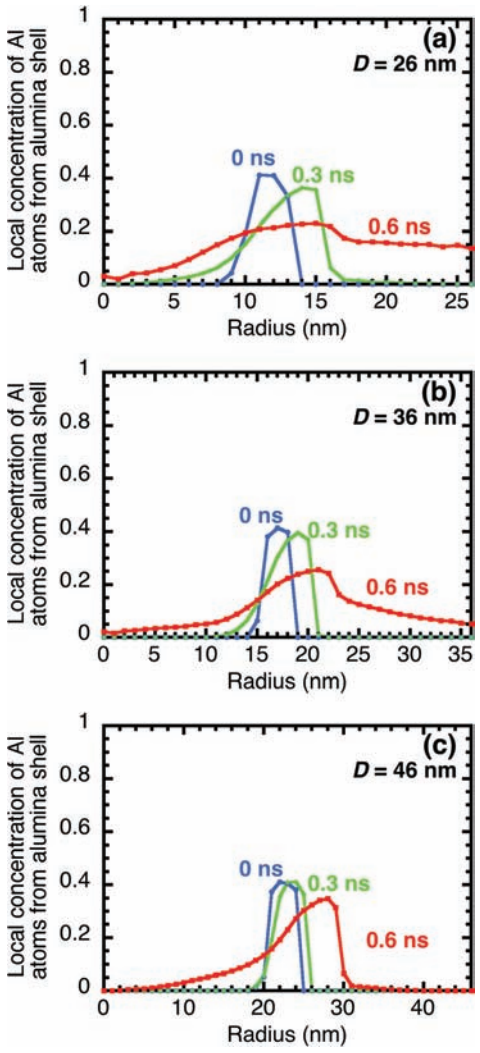

FIG. 8. Local concentration of Al atoms from the alumina shell, C_{Al}^{shell} Eq. (16)), at 0 ns, 0.3 ns and 0.6 ns for (a) $D = 26$ nm, (b) $D = 36$ nm and (c) $D = 46$ nm.

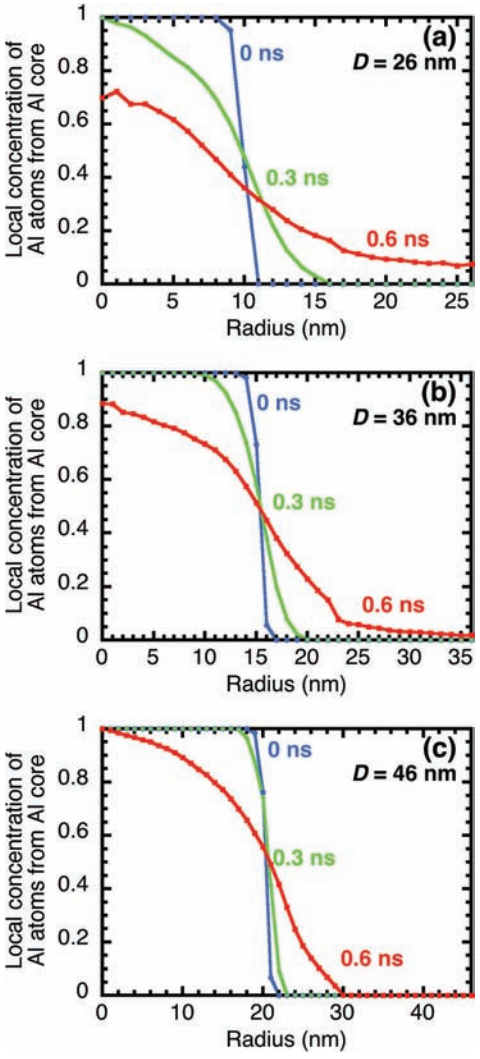

FIG. 9. Local concentration of Al atoms from core, C_{Al}^{core} Eq. (16), at 0 ns, 0.3 ns and 0.6 ns for (a) $D = 26$ nm, (b) $D = 36$ nm and (c) $D = 46$ nm.

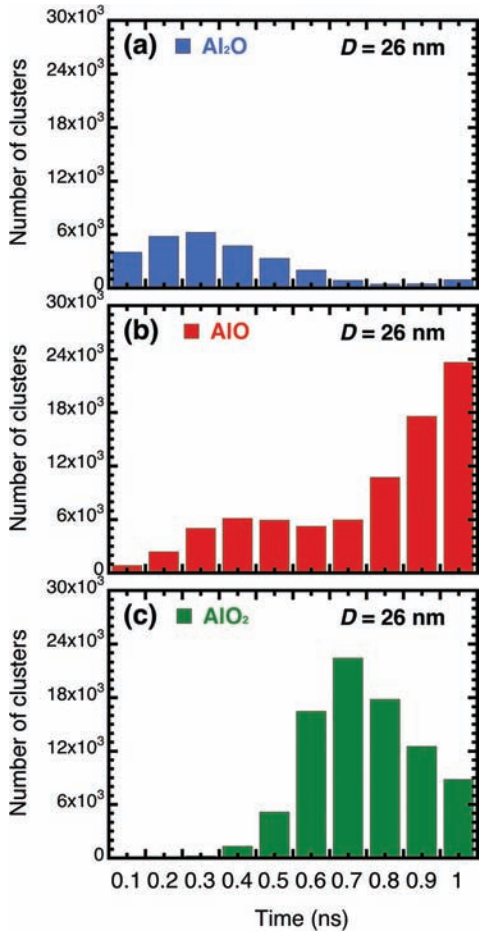

FIG. 10. Number of (a) Al_2O, (b) AlO, and (c) AlO_2 clusters as a function of time in $D = 26$ nm.

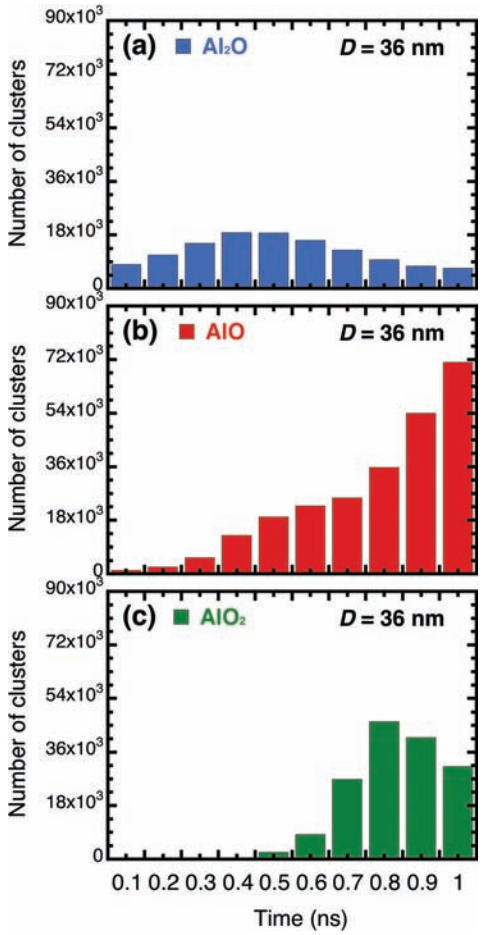

FIG. 11. Number of (a) Al_2O, (b) AlO, and (c) AlO_2 clusters as a function of time in $D = 36$ nm.

which correspond to the oxide shell), in the early stage of the reaction, the majority of fragments in all systems is small clusters, having less than six atoms. Figures 10–12 show the number of clusters Al_2O, AlO and AlO_2 in $D = 26$, 36 and 46 nm, respectively, in the reaction process. We found that, in all three systems, the number of Al_2O clusters (blue) decreases after an initial increase. The AlO (red) and AlO_2 (green) clusters become more numerous after certain times. From the figures, we observe that the majority of the clusters in all three systems changes from Al-rich to oxygen-rich after different time durations. For $D = 26$ nm, the population of AlO exceeds that of Al_2O around 0.3 ns, which is earlier than 0.5 ns for $D = 36$ nm and 0.7 ns for $D = 46$ nm.

E. Evolution of the shell structure

During the oxidation, the shell structure of Al-NPs changes, in width due to core expansion and also in its chemical composition. Figure 13(a) shows the outer radius of the Al-NPs. Within 1 ns, $D = 26$ and 36 nm systems show expansion followed by contraction, whereas 46 nm system only shows expansion. The contraction phase for the $D = 46$ nm system is beyond 1 ns. The extent of expansion (the increment percentage of the radius from the initial value to the maximum value) of the $D = 26$, 36 and 46 nm systems is 18.89%, 22.33% and 24.18%, respectively. The oxide shell radius is calculated by averaging distances from the center of the system to all atoms contained within the largest oxide fragment. Fig. 13(b) shows the ratio between oxygen atoms and aluminum atoms in the largest oxide fragments (i.e., the oxide shell). Initially, the O/Al ratio of 1.5 stands for the amorphous Al_2O_3 shell. The formation of the shell structure is a dynamic process involving Al atoms coming into the shell from the core and Al atoms leaving the shell into the oxygen environment. The overall tendency of the ratio is declining. At early times, the O/Al ratio in the shell region decreases with time for all the three systems. For $D = 26$ nm, oxygen incorporation from the environment increases the ratio until it peaks around 1.45 at 0.5 ns and then decreases. A similar behavior is observed for $D = 36$ and 46 nm, but at later times and with different ratio values. By 1 ns, the ratio for all systems is under 1.4, which means that the largest fragment in the system changes from perfect amorphous oxide shell to an Al-rich shell.

In the process of oxidation, we observe some shell Al atoms eject out into the surrounding oxygen. In order to quantitatively determine the ejection process, after the oxide shell structure has been defined (the largest oxide fragment), we count the number of shell Al atoms that are located beyond the oxide shell radius. Figure 14(a) plots the number of ejected shell Al atoms as a function of time. The onset time for Al ejection from the shell is $t_0 = 0.18$ ns, 0.28 ns and

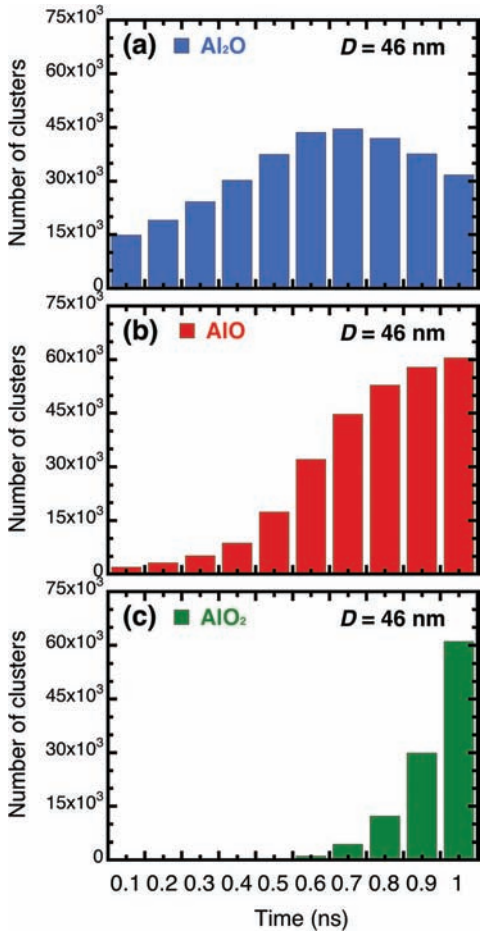

FIG. 12. Number of (a) Al_2O, (b) AlO, and (c) AlO_2 clusters as a function of time in $D = 46$ nm.

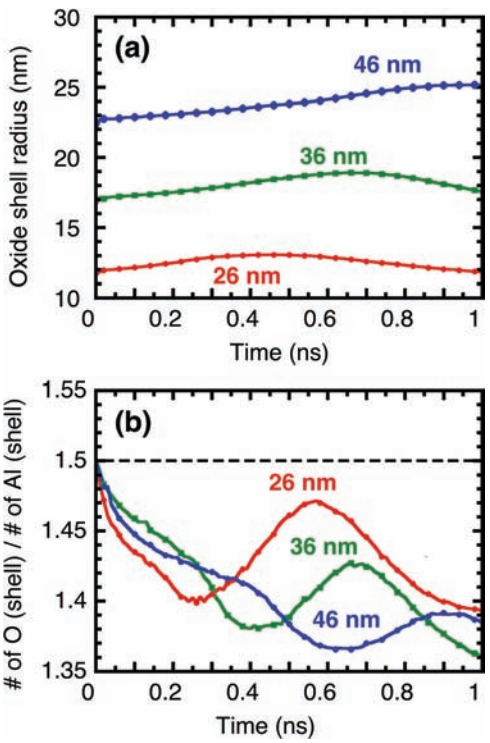

FIG. 13. Different shell structure of $D = 26$, 36 and 46 nm systems are illustrated by (a) the radius of Al-NPs as a function of time, and (b) the ratio of oxygen and aluminum within the shell region.

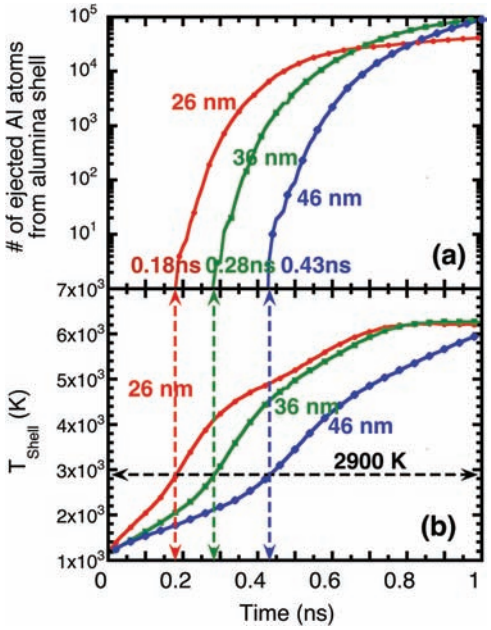

FIG. 14. (a) Semi-log plot of the number of ejected Al shell atoms as a function of time for $D = 26$, 36, and 46 nm. (b) Oxide shell temperature during oxidation as a function of time for the three Al-NP systems. Ejection of Al atoms from the shell starts when the shell is in molten state at 2900 K.

0.43 ns for $D = 26$, 36 and 46 nm, respectively. For $D = 26$ nm, the shell aluminum atoms eject earlier than $D = 36$ and 46 nm, resulting in a faster heat release. This is

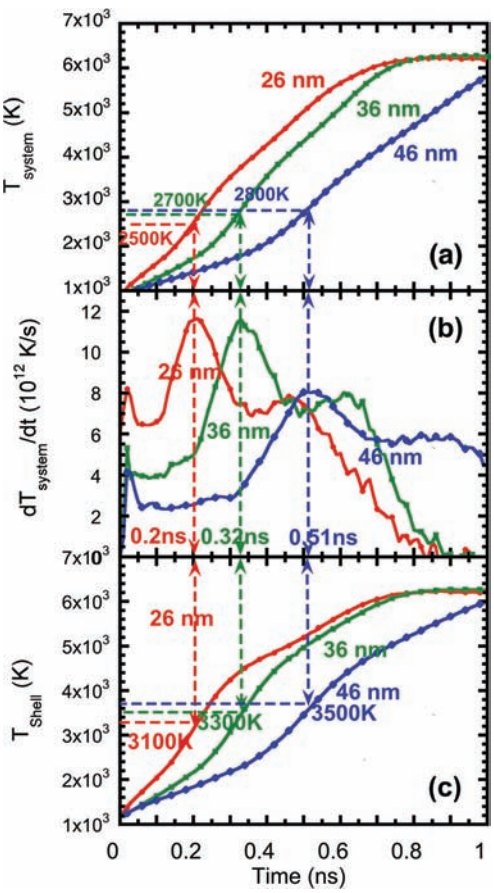

FIG. 15. (a) The global temperature, (b) the rate of change in the global temperature (dT_{system}/dt), and (c) oxide shell temperature as a function of time for $D = 26$, 36 and 46 nm.

TABLE II. Relationship between the delay time and the nanoparticle size.

D, Diameter of the nanoparticle (nm)	t_0, Time for the onset of Al ejection from the shell (ns)	Temperature of the shell at the onset Al ejection (K)	t_1, Peak time of (dT_{system}/dt) (time derivative of the temperature of the whole system) (ns)	Temperature of the shell at peak of (dT_{system}/dt) (K)	Temperature of whole system (including environmental oxygen) at the peak of (dT_{system}/dt) (K)	$t_1 - t_0$, Reaction delay (ns)
26	0.18	2900	0.20	3100	2500	0.02
36	0.28	2900	0.32	3300	2700	0.04
46	0.42	2900	0.51	3500	2800	0.09

reflected as higher global temperature in $D = 26$ nm than in $D = 36$ and 46 nm after the same amount of time as shown in Fig. 14(b), which plots the temperature of oxide shell during oxidation as a function of time. Comparison of Figs. 14(a) and 14(b) shows that for all three Al-NP systems the shell temperature at the onset Al ejection time is the same, i.e., ~2900 K. The dashed arrows specify the onset time of Al ejections as obtained from Fig. 14(a). The black dashed double arrows mark the shell temperature when Al ejections begin. Thus, we conclude that only after the shell temperature reaches 2900 K, the shell Al atoms will start their ejections into the oxygen environment. At 2900 K, the alumina shell is in molten state in all three systems.

F. Reaction delay

In order to explain the time dependence of reaction for the three systems, we plot temperature of Al-NPs including the surrounding oxygen at different time in Fig. 15(a) and the rate of change in temperature (dT_{system}/dt) for the three systems in Fig. 15(b). Comparing Figs. 15(a) and 15(c) (same as Fig. 14(b)), the temperature of the global systems and the oxide shells has the same increasing trend. This restates the fact that the temperature of the shell is higher than the average temperature of the whole system, which indicates that reaction in the core-shell region dominates the heat release as mentioned in Sec. IV A.

Figure 15(b) shows that the largest rate of change in temperature (dT_{system}/dt) occurs at $t_1 = 0.2$ ns, 0.32 ns and 0.51 ns for $D = 26$, 36 and 46 nm, respectively. At these times, the reaction is most intensive. Once passing this peak (i.e., the largest rate of change in temperature $(dT_{system}/dt)_{max}$), temperature still increases but at a slower rate. In Fig. 15(a), the temperature at the culmination point is given for each Al-NP (2500 K, 2700 K and 2800 K for $D = 26$, 36 and 46 nm, respectively).

It is worth noting that the delay of the culmination points from the onset of shell-Al ejection is different for the three Al-NPs systems. The delay for $D = 26$, 36 and 46 nm are $(t_1 - t_0) = 0.02$, 0.04 and 0.09 ns, respectively. Namely, smaller system has shorter delay. Table II shows the detailed comparison of Figs. 15(a) and 15(c).

Finally, we would like to point out the possible effects of oxygen density on the reaction dynamics. In this paper, we used a higher oxygen density so that the entire oxidation process can be observed during the simulation time. We expect that the earlier stage of the reaction is less sensitive to the oxygen density because the reaction is occurring inside the nanoparticle at the metal core and oxide shell. However, the reaction at the later stage involves the environmental oxygen, thus it should depend on the oxygen density.[51] This can be seen in the $D = 26$ nm Al-NP, where the depletion of environmental oxygen slows down the oxidation reaction. From Fig. 15(b), the oxygen from the environment for 26 nm system is almost consumed after 0.6 ns, which leads to a decrease of the reaction rate (dT_{system}/dt), as shown in Fig. 15(c).

V. CONCLUSION

Reactive MD simulations results have provided quantitative information on the mechano-chemistry and the atomistic mechanism of oxidation for Al-NPs of different sizes, $D = 26$, 36 and 46 nm in which the Al core diameter is varied from 20 to 40 nm and the alumina shell thickness is held constant at 3 nm. In the initial state of the system, the nanoparticles are uniformly heated to 1100 K in ambient oxygen environment.

We find that the oxidation dynamics starts within the Al-NP at the core-shell interface when molten aluminum starts reacting with alumina shell by taking some oxygen from expanded alumina shell to form aluminum rich Al_xO_y $(x > y)$ clusters. This reaction at the aluminum/alumina interface generates heat first. By analyzing the structure of the oxide shell of all three Al-NPs in the process of this reaction, we found that the shell of Al-NPs does not break or shatter, but only deforms, where the deformations differ slightly depending on the size of the Al-NP. For smaller Al-NP, which has larger surface-to-volume ratio and lower ratio of core-radius-to-shell-thickness, the reaction is faster. In early stage of the reaction, a majority of Al_xO_y clusters formed are small, having less than six atoms. Most of the clusters in this stage are AlO and Al_2O as shown in Figs. 10–12. The induced heat is mainly as a result of the oxidation dynamics at the aluminum/alumina interface. When the temperature reaches ~2900 K, the alumina shell melts. This shell melting is coincident with the start of aluminum ejections from the Al-NP into oxygen environment. The aluminum ejections start earlier in smaller Al-NP—at $t_0 = 0.18$, 0.28 and 0.42 ns for $D = 26$, 36 and 46 nm. We would like to emphasize here that in all the three systems the shell temperature at $t_0 = 0.18$, 0.28, and 0.42 ns is 2900 K at which time the shell is in molten state. After the Al ejection starts from Al-NP, the oxidation dynamics also starts at the alumina/oxygen

interface. The initial Al_xO_y clusters found in this outer region are oxygen rich ($y > x$). The start time of AlO_2 clusters production in the outer regions of the Al-NP is after the shell temperature has reached ~2900 K, as can be inferred from Figs. 10(c)–12(c). We have also examined the rate of heat production in the three Al-NP systems. As the oxidation proceeds, the total system temperature (including the environmental oxygen) increases monotonically; however, the time derivative of the total system temperature, (dT_{system}/dt), has a peak that occurs at $t_1 = 0.20$, 0.32 and 0.51 ns for $D = 26$, 36 and 46 nm. At this peak in the time derivative of the total temperature, in (dT_{system}/dt), the shell temperature for the three Al-NPs is 3100 K, 3300 K, and 3500 K, respectively, as given in Table II. However, because all the oxygen is not uniformly heated due to continuing oxidation dynamics inside and outside the Al-NP, the full system temperature is lower than the shell temperature. At the peak in (dT_{system}/dt), the system temperature for the three Al-NP systems is 2500 K, 2700 K, and 2800 K, respectively. The time lag between when the shell temperature reaches ~2900 K and the peak in time derivative of the total system temperature, (dT_{system}/dt) specifies maximum rate of heat production is $t_1 - t_0 = 0.02$, 0.04 and 0.09 ns for $D = 26$, 36 and 46 nm, clearly indicating the Al-NP size effect.

ACKNOWLEDGMENTS

This research work was started with the support by the Basic Research Program of Defense Threat Reduction Agency (DTRA) Grant No. HDTRA1-08-1-0036 and the research was completed with the support from the Office of Naval research (ONR) Grant No. N000014-12-1-0555. All the simulations were performed at the Center for High Performance Computing and Communications at USC.

[1]E. L. Dreizin, Combust. Flame **105**, 541 (1996).
[2]J. L. Jordan, L. Ferranti, R. A. Austin, R. D. Dick, J. R. Foley, N. N. Thadhani, D. L. McDowell, and D. J. Benson, J. Appl. Phys. **101**, 093520 (2007).
[3]K. Brandstadt, D. L. Frost, and J. A. Kozinski, Proc. Combust. Inst. **32**, 1913 (2009).
[4]A. Ermoline, M. Schoenitz, and E. L. Dreizin, Combust. Flame **158**, 1076 (2011).
[5]M. A. Trunov, M. Schoenitz, X. Y. Zhu, and E. L. Dreizin, Combust. Flame **140**, 310 (2005).
[6]V. I. Levitas, Combust. Flame **156**, 543 (2009).
[7]E. Stratakis, M. Barberoglou, C. Fotakis, G. Viau, C. Garcia, and G. A. Shafeev, Opt. Express **17**, 12650 (2009).
[8]B. S. Bockmon, M. L. Pantoya, S. F. Son, B. W. Asay, and J. T. Mang, J. Appl. Phys. **98**, 064903 (2005).
[9]Z. X. Yan, J. H. Wu, S. Ye, D. Hu, and X. D. Yang, J. Appl. Phys. **101**, 024905 (2007).
[10]S. F. Wang, Y. Q. Yang, H. N. Yu, and D. D. Dlott, Propellants, Explos., Pyrotech. **30**, 148 (2005).
[11]M. Jones, C. H. Li, A. Afjeh, and G. P. Peterson, Nanoscale Res. Lett. **6**, 246 (2011).
[12]J. Gesner, M. L. Pantoya, and V. I. Levitas, Combust. Flame **159**, 3448 (2012).
[13]D. A. Firmansyah, K. Sullivan, K. S. Lee, Y. H. Kim, R. Zahaf, M. R. Zachariah, and D. Lee, J. Phys. Chem. C **116**, 404 (2012).
[14]R. W. Conner and D. D. Dlott, J. Phys. Chem. C **116**, 2751 (2012).
[15]W. K. Lewis, C. G. Rumchik, M. J. Smith, K. A. S. Fernando, C. A. Crouse, J. E. Spowart, E. A. Guliants, and C. E. Bunker, J. Appl. Phys. **113**, 044907 (2013).
[16]Y. Huang, G. A. Risha, V. Yang, and R. A. Yetter, *Proc. Combust. Inst.* 31, 2001 (2007).
[17]Y. S. Kwon, A. A. Gromov, A. P. Ilyin, E. M. Popenko, and G. H. Rim, Combust. Flame **133**, 385 (2003).
[18]V. I. Levitas, B. W. Asay, S. F. Son, and M. Pantoya, Appl. Phys. Lett. **89**, 071909 (2006).
[19]B. Dikici, S. W. Dean, M. L. Pantoya, V. I. Levitas, and R. J. Jouet, Energy Fuels **23**, 4231 (2009).
[20]L. T. De Luca, L. Galfetti, F. Severini, L. Meda, G. Marra, A. B. Vorozhtsov, V. S. Sedoi, and V. A. Babuk, Combust., Explos. Shock Waves **41**, 680 (2005).
[21]K. Jayaraman, K. V. Anand, D. S. Bhatt, S. R. Chakravarthy, and R. Sarathi, J. Propul. Power **25**, 471 (2009).
[22]Y. Huang, G. A. Risha, V. Yang, and R. A. Yetter, Combust. Flame **156**, 5 (2009).
[23]A. B. Morgan, J. D. Wolf, E. A. Guliants, K. A. S. Fernando, and W. K. Lewis, Thermochim. Acta **488**, 1 (2009).
[24]A. N. Pivkina, Y. V. Frolov, and D. A. Ivanov, Combust., Explos. Shock Waves **43**, 51 (2007).
[25]K. Moore, M. L. Pantoya, and S. F. Son, J. Propul. Power **23**, 181 (2007).
[26]Z. X. Yan, J. Deng, and Z. M. Luo, Mater. Charact. **61**, 198 (2010).
[27]T. Bazyn, P. Lynch, H. Krier, and N. Glumac, Propellants, Explos., Pyrotech. **35**, 93 (2010).
[28]K. Park, D. Lee, A. Rai, D. Mukherjee, and M. R. Zachariah, J. Phys. Chem. B **109**, 7290 (2005).
[29]S. W. Chung, E. A. Guliants, C. E. Bunker, P. A. Jelliss, and S. W. Buckner, J. Phys. Chem. Solids **72**, 719 (2011).
[30]Y. A. Gan and L. Qiao, Combust. Flame **158**, 354 (2011).
[31]R. A. Yetter, G. A. Risha, and S. F. Son, Proc. Combust. Inst. **32**, 1819 (2009).
[32]T. Campbell, R. K. Kalia, A. Nakano, P. Vashishta, S. Ogata, and S. Rodgers, Phys. Rev. Lett. **82**, 4866 (1999).
[33]T. J. Campbell, G. Aral, S. Ogata, R. K. Kalia, A. Nakano, and P. Vashishta, Phys. Rev. B **71**, 205413 (2005).
[34]S. Alavi, J. W. Mintmire, and D. L. Thompson, J. Phys. Chem. B **109**, 209 (2005).
[35]F. H. Streitz and J. W. Mintmire, Phys. Rev. B **50**, 11996 (1994).
[36]D. J. Keffer and J. W. Mintmire, Int. J. Quantum Chem. **80**, 733 (2000).
[37]P. Puri and V. Yang, J. Nanopart. Res. **12**, 2989 (2010).
[38]A. Perron, S. Garruchet, O. Politano, G. Aral, and V. Vignal, J. Phys. Chem. Solids **71**, 119 (2010).
[39]G. Gutierrez, A. Taga, and B. Johansson, Phys. Rev. B **65**, 012101 (2002).
[40]G. Gutierrez and B. Johansson, Phys. Rev. B **65**, 104202 (2002).
[41]P. Vashishta, R. K. Kalia, A. Nakano, and J. P. Rino, J. Appl. Phys. **103**, 083504 (2008).
[42]S. P. Chen, A. F. Voter, and D. J. Srolovitz, J. Phys. **49**, 157 (1988).
[43]W. Q. Wang, R. Clark, A. Nakano, R. K. Kalia, and P. Vashishta, Appl. Phys. Lett. **95**, 261901 (2009).
[44]W. Q. Wang, R. Clark, A. Nakano, R. K. Kalia, and P. Vashishta, Appl. Phys. Lett. **96**, 181906 (2010).
[45]A. Shekhar, W. Q. Wang, R. Clark, R. K. Kalia, A. Nakano, and P. Vashishta, Appl. Phys. Lett. **102**, 221904 (2013).
[46]W. Wang, "Thermal properties of silicon carbide and combustion mechanisms of aluminum nanoparticle," Department of Materials Science, University of Southern California, 2008.
[47]A. Hasnaoui, O. Politano, J. M. Salazar, G. Aral, R. K. Kalia, A. Nakano, and P. Vashishta, Surf. Sci. **579**, 47 (2005).
[48]T. N. Piehler, F. C. DeLucia, C. A. Munson, B. E. Homan, A. W. Miziolek, and K. L. McNesby, Appl. Opt. **44**, 3654 (2005).
[49]S. F. Wang, Y. Q. Yang, Z. Y. Sun, and D. D. Dlott, Chem. Phys. Lett. **368**, 189 (2003).
[50]G. I. Pangilinan and T. P. Russell, J. Chem. Phys. **111**, 445 (1999).
[51]J. L. Prentice, J. Electrochem. Soc. **122**, 260 (1975).